Slice-selective excitation with B_1^+-insensitive composite pulses

Jay Moore [a,b,*], Marcin Jankiewicz [a,b], Adam W. Anderson [a,b,c], John C. Gore [a,b,c]

[a] Vanderbilt University Institute of Imaging Science, 1161 21st Ave. South, MCN AA-1105, Nashville, TN 37232-2310, USA
[b] Department of Radiology and Radiological Sciences, Vanderbilt University, 116 21st Ave. South, MCN CCC-1106, Nashville, TN 37232-2675, USA
[c] Department of Biomedical Engineering, Vanderbilt University, 5824 Stevenson Center, VU Station B 351631, Nashville, TN 37232, USA

ARTICLE INFO

ABSTRACT

Spatially selective excitation pulses have been designed to produce uniform flip angles in the presence of the RF and static field inhomogeneities typically encountered in MRI studies of the human brain at 7 T. Pulse designs are based upon non-selective, composite pulses numerically optimized for the desired performance over prescribed ranges of field inhomogeneities. The non-selective pulses are subsequently transformed into spatially selective pulses with the same field-insensitive properties through modification of the spectral composition of the individual sub-pulses which are then executed in conjunction with an oscillating gradient waveform. An in-depth analysis of the performance of these RF pulses is presented in terms of total pulse durations, slice profiles, linearity of in-slice magnetization phase, sensitivity to RF and static field variations, and signal loss due to T_2^* effects. Both simulations and measurements in phantoms and in the human brain are used to evaluate pulses with nominal flip angles of 45° and 90°. Target slice thickness in all cases is 2 mm. Results indicate that the described class of field-insensitive RF pulses is capable of improving flip-angle uniformity in 7 T human brain imaging. There appears to be a subset of pulses with durations $\lesssim 10$ ms for which non-linearities in the magnetization phase are minimal and signal loss due to T_2^* decay is not prohibitive. Such pulses represent practical solutions for achieving uniform flip angles in the presence of the large field inhomogeneities common to high-field human imaging and help to better establish the performance limits of high-field imaging systems with single-channel transmission.

1. Introduction

The problem of spatially-dependent signal variations arising from non-uniformities in the strength of the transmitted radio frequency field (B_1^+) [1] has received much attention over the last decade due to the proliferation of high-field ($\geqslant 3$ T) magnets for human MR imaging and spectroscopy. The challenge of mitigating such signal variations in order to better realize the potential of high-field imaging systems has sparked a renewed interest in the design of RF pulses that invoke a magnetization response insensitive to the B_1^+ field strength [2–11]. Due to non-selective frequency profiles and non-linear transverse magnetization phase in the through-slice direction, many such pulses are limited in application to whole-volume acquisitions. Related pulse designs that could provide the B_1^+-insensitivity needed for high-field applications while additionally permitting slice-selective imaging by way of a gradient-recalled echo (GRE) are therefore of interest. Design criteria for such a class of pulses are extensive and include: (1) durations short enough to avoid significant T_2^* signal loss at 7 T; (2)

bandwidths suitable for imaging thin ($\lesssim 5$ mm) slices without slice profile distortions due to in-plane B_0 variations; (3) linear (or quasi-linear) through-slice magnetization phase profiles that allow for rephasing using linear gradients (i.e., GRE); (4) slice profiles suitable for highly selective imaging (i.e., profiles comparable to those attained with Gaussian or apodized sinc pulses); (5) peak amplitudes consistent with the performance limits of typical RF amplifiers used by clinical scanner manufacturers; and (6) average RF power levels that permit safe scanning of human subjects given the currently accepted limits on specific absorption rates (SAR $\leqslant 3$ W/kg in the brain [12]).

Although the above requirements for B_1^+-insensitive slice selection are daunting, progress has been made recently in the development of such pulses. In 1993, a gradient modulation technique was demonstrated as a means for achieving spatial selectivity for composite excitation pulses [13]. The technique relied upon a series of gradient lobes of alternating polarity—each of which was responsible for allowing the spatial selectivity of a given sub-pulse in the composite waveform while simultaneously rephasing the magnetization produced by the prior sub-pulse. Today, this approach is widely adopted in the design of sparse spokes pulses used for flip-angle inhomogeneity corrections [14,15] but has proven adaptable to other pulse types. In 2008, Balchandani et al. [8] used

* Corresponding author at: Vanderbilt University Institute of Imaging Science, 1161 21st Ave. South, MCN AA-1105, Nashville, TN 37232-2310, USA.
E-mail address: jay.moore@vanderbilt.edu (J. Moore).

such oscillating selection gradients to transform a non-selective BIR-4 excitation pulse into a spatially selective pulse with similar B_1^+-insensitive properties. In this technique, BIR-4 phase and amplitude modulation patterns served as envelopes defining the phases and amplitudes of a train of spectrally selective sub-pulses formed from the central lobes of sinc functions (hereafter referred to as sinc modulation). In the context of a GRE sequence with a 90° excitation, the study showed improvements in flip-angle uniformity for 10 mm slice thicknesses in a phantom and the *in vivo* human brain at 3 T and represents a significant step in advancing the limits of practical single-channel pulse designs.

The work presented here uses the same spatial selectivity strategy as that discussed above but in conjunction with composite pulses designed to produce uniform flip angles over specified ranges of B_0 and B_1^+ field strengths [10] and is thus akin to recent work by Matson et al. [16] and Boulant et al. [17]. In general, this class of composite pulses is characterized by non-selective composite pulses numerically optimized for insensitivity to field variations and subsequently endowed with spectral selectivity via the use of shaped sub-pulses, e.g., Gaussian (hereafter referred to as GAU) or sinc sub-pulses. Furthermore, optimization cost functions do not rely explicitly on fulfillment of the adiabatic condition to achieve immunity to B_1^+ variations. This latter characteristic is potentially advantageous given that the pulse durations and high RF power needed for adiabaticity are not always attainable in the human brain at 7 T due to the combination of large B_1^+ variations, RF amplifiers with limited peak amplitudes, SAR restrictions, and relatively short T_2^* values. In addition to corroborating the findings of existing works (i.e., [8,16,17]), the present study uniquely contributes to the knowledge of such pulse designs through investigating (1) the efficacy of an alternative optimization protocol, (2) the use of higher gradient strengths for achieving imaging slice thicknesses of ~2 mm, (3) the slice profile variations resulting from different sub-pulse amplitude modulations (i.e., GAU and sinc), (4) the use of a wide range of total pulse durations (~2–20 ms) so as to explore the potential trade-off between pulse performance (i.e., insensitivity to B_1^+ and B_0 variations) and relaxation effects (i.e., T_2^* and $T_{2,\rho}$ [18,19]), and (5) the application of such pulses to multiple subjects without using subject specific optimizations.

Given these specific objectives, the underlying motive of the present study was to further test the limitations of single-channel, slice-selective pulse designs for practical use at 7 T. While multi-transmit technologies promise to meet many of the same needs, single-channel pulse designs are very much of interest given that all scanners are not yet equipped with multi-transmit hardware and that the SAR demands of multi-transmit systems have not been fully established. Furthermore, the pulses of this study have an inherent advantage over current multi-transmit methods in that subject-specific field maps and subsequent pulse calibrations do not have to be made—pulses are designed with the goal of delivering the required performance despite widespread differences in B_0 and B_1^+ field geometries.

2. Methods

The description of methods is presented in three main parts: pulse designs, simulations, and experiments.

2.1. Pulse designs

2.1.1. Structure and optimization of non-selective pulses
The first step of the pulse design process was to generate non-selective composite pulses with inherent insensitivity to variations in the B_0 and B_1^+ fields. This was accomplished with a pre-existing protocol [10] for numerical optimization that employs a discrete

grid of relevant ΔB_0 and B_1^+ values. The ΔB_0 and B_1^+ ranges of this grid were chosen to be ±150 Hz and [0.25, 1.00], respectively, with the latter being in units of the nominal B_1^+ field strength $\left(B_{1,\text{nom}}^+\right)$. These choices designate the field variations over which the resulting pulse is required to perform and were guided by the previous 7 T study [10]. Field ranges were discretized into 31 steps in the ΔB_0 direction (resulting in steps of 10 Hz) and 16 steps in the B_1^+ direction (resulting in steps equivalent to 5% increments of $B_{1,\text{nom}}^+$). The resulting B_1^+-ΔB_0 grid provided a visualization tool when magnetization response to a given RF pulse was simulated and also served as a basis for formulating the numerical optimization problem.

Just like those from our previous work [10], the non-selective pulses of the present study consist of sub-pulses with constant phase and amplitude; however, the new pulses differ from the previous ones in that (1) sub-pulse duration was significantly lengthened to accommodate the substitution of GAU and sinc modulations needed for slice selection and (2) peak RF amplitudes were further limited such that necessary amplitude adjustments for the slice-selective sub-pulses could be made without exceeding the peak RF limit of 15 μT. These constraints resulted in sub-pulse durations of 665.6 μs and 1062.4 μs (integer multiples of the digital RF amplifier's dwell time of 6.4 μs) and maximum amplitudes of 8.8 μT and 5.0 μT for the sinc and GAU formats, respectively. Motivation for these particular duration and amplitude values is further described in Section 2.1.2.

With sub-pulse durations and maximum amplitude values fixed, the k phases ($\phi = \{\phi_1, \phi_2, \ldots, \phi_k\}$) and k amplitudes ($\mathbf{A} = \{A_1, A_2, \ldots, A_k\}$) of a given sequence of block-shaped sub-pulses were determined through minimization of the cost function

$$\delta_\alpha(\mathbf{A}, \phi) = \frac{1}{m \cdot n} \sum_{i,j=1}^{m,n} \left| \frac{\alpha_{i,j}^S(\mathbf{A}, \phi) - \alpha_{i,j}^T}{\alpha_{i,j}^T} \right|, \tag{1}$$

where i is the B_1^+ index (with m = 16) on the B_1^+-ΔB_0 grid, j is the ΔB_0 index (with n = 31) on the B_1^+-ΔB_0 grid, and α is the flip angle given by $\cos^{-1}(M_z/M_0)$ with S and T denoting simulated and target values. In this study, $\alpha_{i,j}^T$ values were set to either 45° or 90° over the entire optimization grid, thus prescribing uniform flip angles over the specified ranges of field variations. The value of δ_α represents the average deviation of simulated flip angles from the target flip angle over the entire B_1^+-ΔB_0 grid and is expressed as a fraction of the target flip angle. Solutions to the minimization problem were found using the fmincon function in Matlab (The MathWorks, Natick, MA, USA) with the interior-point algorithm. This constrained minimization technique involves numerical approximations to the Hessian of the LaGrangian of δ_α in combination with a series of linear and conjugate-gradient steps. Initial conditions for all optimizations were defined by randomly assigned phase and amplitude values for each sub-pulse (within the constraints of $-\pi \leqslant \phi_k \leqslant +\pi$ and $0 \leqslant A_k \leqslant 15$ μT) and an initial magnetization vector of $\mathbf{M}_0 = (M_x, M_y, M_z) = (0, 0, 1)$. The numerical optimization was carried out for four categories of pulses corresponding to the two target flip angles (45° and 90°) and the two amplitude/duration formats (GAU and sinc) described above. Within each category, composite pulses were generated with k = 1, 2, ..., 19 sub-pulses, thus reflecting the desired range of total pulse durations to be investigated, i.e., $\Delta T \sim$ 1–20 ms (see Section 2.1).

Despite the relatively low number of free parameters in the optimization problem (e.g., the maximum number is 40 in the case of 20 sub-pulses), the minimization algorithm was found to be rather sensitive to initial conditions. To ensure avoidance of outlying local minima, the optimization was repeated 100 times for each pulse as defined by a unique combination of target flip angle (α^T), total duration (ΔT), sub-pulse duration, and maximum sub-pulse amplitude values. Only phase and amplitude sets resulting in the lowest value of δ_α for a given pulse structure were considered in

the subsequent analysis of pulse performance. An example of the observed sensitivity to initial conditions for one pulse structure is shown in Fig. 1 and helps to justify the repetition of optimizations. Computational time varied for pulses of different durations, but, in general, optimizations for a single set of initial conditions were performed in less than a minute on a desktop computer.

2.1.2. Construction of slice-selective pulses

Non-selective composite pulses were translated into slice-selective pulses by replacing the block-shaped amplitude modulations with either GAU or SINC waveforms of the same duration and then synchronizing the pulse train with a bipolar slice-selection gradient. The peak amplitude of each GAU/SINC sub-pulse was adjusted such that the integrated amplitude (or, equivalently, flip angle as given by $\int \gamma A_k dt$) was left unchanged relative to that of the corresponding block-shaped sub-pulse. Sub-pulse phases were not adjusted in the translation from non-selective to slice-selective pulses. Given a desired slice thickness of 2 mm and a maximum gradient strength of 33 mT/m, the relationship

$$\Delta z = BW/(\gamma \cdot G), \tag{2}$$

where Δz is slice thickness, BW is the bandwidth of the RF pulse, G is the gradient strength, and $\gamma = 42.57$ MHz/T is the gyromagnetic ratio for ^{1}H, necessitates RF bandwidths of $\sim$2800 Hz. According to slice profile criteria described previously [20], the standard deviation of the GAU sub-pulses in this study was fixed to 13.5% of the total sub-pulse duration. The SINC sub-pulses were determined using the `firls` function in Matlab according to Balchandani et al. [8]. The target bandwidth in conjunction with these particular amplitude modulations led to the choice of the 665.6 μs and 1062.4 μs durations for the SINC and GAU sub-pulses.

Fig. 2 shows simulated slice profiles for individual GAU and SINC waveforms when executed in the presence of a trapezoidal gradient. The gradient has a total duration equal to that of the GAU pulse. Peak gradient amplitude (33 mT/m) and slew rate (166 T/m/s) correspond to the maximum available on the Philips 7 T system at the time of this study. The RF and gradient waveforms shown in Fig. 2 are identical in structure to those concatenated to form all slice-selective composite pulses appearing in this study.
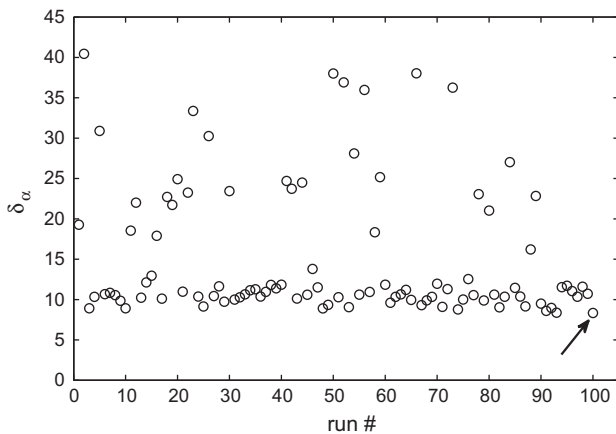
Fig. 1. Optimization performance (δ_α, Eq. (1)) as a function of run number for a 13-element composite pulse with a target flip angle of 45° and a maximum amplitude of 8.8 μT, as is the case for SINC pulse format. Runs represent identical optimizations with different random initial conditions (i.e., random initial sub-pulse phases and amplitudes). The arrow indicates the run with lowest δ_α which was selected to represent pulses of the given composition and is reported in Fig. 3. Although the majority of runs converge to $\delta_\alpha \sim 10$, this minimization problem with 26 free-parameters clearly demonstrates a sensitivity to initial conditions that warrants repeating the optimization to check for the possibility of a more favorable starting point.

2.2. Simulations

Magnetization response to the non-selective composites of k sub-pulses with constant phase and amplitude were modeled as a series of rotations (R_j, where $j = 1, \ldots, k$), as described by the relaxation-independent form of the Bloch equation [21]. With each rotation corresponding to one of the k individual sub-pulses, the collective operation of all components of a composite pulse is described by

$$\mathbf{M} = R_k R_{k-1} R_{k-2} \ldots R_1 \mathbf{M}_0, \tag{3}$$

where $\mathbf{M}_0$ is the magnetization vector preceding the pulse and $\mathbf{M}$ is the magnetization vector following the pulse. During optimizations, magnetization response was simulated over the B_1^+-ΔB_0 grids of the dimensions described in Section 2.1; however, simulation data presented in this manuscript were calculated over grids with much higher resolution (i.e., 1% and 1 Hz increments in the $B_1^+/B_{1,\,nom}^+$ and ΔB_0 directions, respectively).

Simulations of the Bloch equation for slice-selective composite pulses were performed using the same methods as for non-selective pulses except that each of the k sub-pulses was further discretized into l parts (with l being the number of 6.4 μs intervals within the sub-pulse) over which RF amplitude, RF phase, and gradient strength were considered constant. Thus, an entire composite pulse required $k \times l$ rotation operators, such that each R_k in Eq. (3) is expressible as

$$R_k = R_{k,l} R_{k,l-1} R_{k,l-2} \ldots R_{k,1}. \tag{4}$$

Such simulations resulted in magnetization responses that were illustrated on high-resolution B_1^+-z grids, with z denoting position along the slice-selection direction. Magnetization was calculated in this way over a range of ±5 mm, thus well beyond the target slice thickness. The large number of rotation operators was not prohibitive in this case since all optimizations were performed only for non-selective pulses.

To evaluate the dependence of magnetization on the decay constant T_2^* during application of a given RF pulse, the Bloch equation was simulated with relaxation effects included. To accomplish this, a finite difference method was adopted for which the iterative cycle was 100 times shorter than the 6.4 μs interval used for relaxation-free simulations. Such short increments proved necessary to ensure realistic behavior of the simulated magnetization response.

In order to further establish practical limitations, a set of values reflecting SAR and echo time constraints were calculated for each pulse. These values include the integral of the square of the amplitude (a quantity directly proportional to SAR), the minimum allowed repetition time given the SAR constraint of 3 W/kg ($T_{R,min}$), and the minimum possible echo time ($T_{E,min}$). The first of these is a straightforward calculation involving the amplitude modulation of the slice-selective version of each pulse. The second value, $T_{R,min}$, is determined from inverting the relationship

$$SAR = \frac{C}{T_R} \int_0^{\Delta T} |A(t)|^2 dt, \tag{5}$$

in which $A(t)$ is the amplitude modulation function and C is a coil specific constant describing the rate of energy dissipation of 298 MHz radiation in human brain tissue. The value $T_{E,min}$ is determined by taking half of the total pulse duration and adding the time needed for a rephasing gradient of the same duration as a single sub-pulse. This reflects the way minimum echo times are typically calculated by commercial MR scanner software.
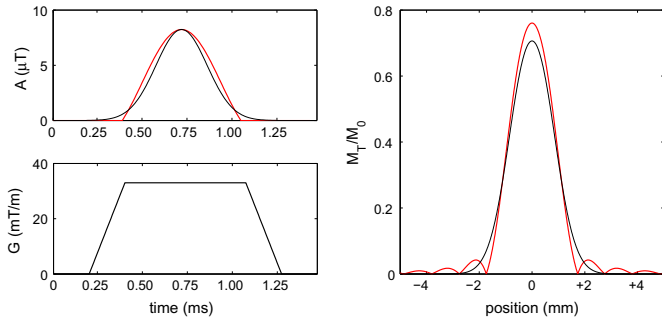
Fig. 2. Simulated slice profiles (right) for Gaussian (black) and central-sinc lobe (red) RF waveforms (top left) of the same bandwidth executed in the presence of the given 33 mT/m slice-selection gradient (bottom left). The Gaussian pulse has the same total duration as the trapezoidal gradient. The duration of the sinc pulse is the same as that of the gradient plateau. In both cases, the slice thickness is 2 mm at half of the maximum M_T/M_0 value. (For interpretation of the references to colour in this figure legend, the reader is referred to the web version of this article.)

2.3. Experiments

All experiments were conducted on a 7 T Philips Achieva whole body scanner (Philips Healthcare, Best, Netherlands) based on a Magnex (Agilent Technologies, Santa Clara, CA) 90 cm magnet. RF transmission and reception were carried out with a single-channel, quadrature volume head coil from Nova Medical (Wilmington, MA). A 17 cm dielectric phantom from FBIRN (Function Biomedical Information Research Network) with relaxation constants of $T_1/T_2^* = 1150/42$ ms (as measured at 7 T) was used for all phantom experiments. For *in vivo* experiments, three healthy volunteers were recruited from the community, and written informed consent was obtained for each according to the guidelines of the local Institutional Review Board.

Static field maps were obtained in the phantom and human subjects using a 2D GRE sequence with a double-echo acquisition ($\Delta T_E = 1$ ms), a repetition time (T_R) of 5 ms, and a flip angle of 10°. Slice orientation was axial, and scan resolution was 3×3 mm within a 240×192 mm field of field in the anterior-posterior and right-left directions, respectively. Slice thickness was 2 mm, corresponding to the target slice thickness of the pulses in this study. The same projection-based, second-order, volume B_0 shims were used during this and all subsequent scans.

Maps of $B_1^+/B_{1,nom}^+$ and $M_0 B_1^-$ were calculated via a voxel-by-voxel, fitting of signal intensities from a multi-flip-angle, multi-slice, multi-shot (3 lines of k-space per shot) GRE-EPI scan with a T_R of 5 s [15,22]. Given that the signal resulting from a long-T_R, short-T_E GRE sequence employing an excitation pulse with no phase/frequency modulation is expressible as

$$S = \beta F = \beta |\sin \lambda \alpha_0|, \tag{6}$$

where β represents the product of the equilibrium magnetization (M_0) and the relative intensity of the RF field associated with the receiver coil (B_1^-), λ represents the relative strength of the transmitted RF field $\left(B_1^+/B_{1,nom}^+\right)$ and α_0 is the nominal flip angle, the fitting procedure of the B_1^+ measurement technique resulted in estimates of both β and λ. While λ reflects actual variations in B_1^+, the parameter β was used for evaluating the uniformity of excitations produced by the various RF pulses as described below. In-plane resolution, slice thickness, and field of view of the B_1 scan were matched to those of the ΔB_0 scan. Prior to the multi-flip-angle fitting procedure, B_0 maps were used to perform EPI distortion corrections of the B_1 scan data [23].

Imaging experiments for evaluating pulse performance employed the same 2D GRE sequence as used for B_1^+ mapping. In order to reflect the practical limitations associated with pulses of

different duration, echo time (T_E) was set to the shortest possible value for a given excitation pulse. This resulted in signal acquisitions that began ~1 ms after the end of any given RF excitation, thus allowing time for the rephasing gradient which was in all cases the same length but half the strength of the individual gradient lobes used during application of the RF pulse. Imaging experiments were performed for only a small sample of the 80 pulses derived in this work. In addition to 45° and 90° single-Gaussian pulses, only the pulses circled in Fig. 3—namely, the GAU and SINC pulses with 5 and 8 components (hereafter referred to using the abbreviations 5-GAU, 8-GAU, 5-SINC, and 8-SINC)—were implemented on the scanner. While all of these pulses were tested on the phantom, only the 1-GAU and 5-SINC pulses were tested in the brain. As a measure of the flip-angle uniformity produced by each pulse, both phantom and *in vivo* images (comprising S in Eq. (6)) were divided on a voxel-by-voxel basis by the corresponding map of β as derived from the B_1^+-mapping procedures—thus producing maps of the flip-angle dependent function F in Eq. (6). Prior to division, both images and β maps were normalized to their respective values at locations for which $B_1^+/B_{1,nom}^+ = 1$. This normalization step facilitates the evaluation of flip-angle homogeneity for excitation pulses other than the one used in the B_1^+-mapping sequence but, due to uncertainties involving slice profiles and the measurement of β, may result in values of F that exceed unity. Although such values are not physical in the context of Eq. (6), they are still meaningful for characterizing the uniformity of a given excitation. An alternative approach would be to adjust signal intensities based on the slice-profile measurements described below; however, this procedure was avoided since it would rely upon additional measurements that incorporate additional sources of error.

To verify target slice thickness, slice profiles were measured in the same phantom for all pulses used in the previously described imaging experiments. For this purpose, the phase-encoding of the read-out was oriented along the slice-selection direction in a 2D GRE sequence. All other scan parameters were the same as those of the 2D GRE sequence adopted for imaging experiments, with
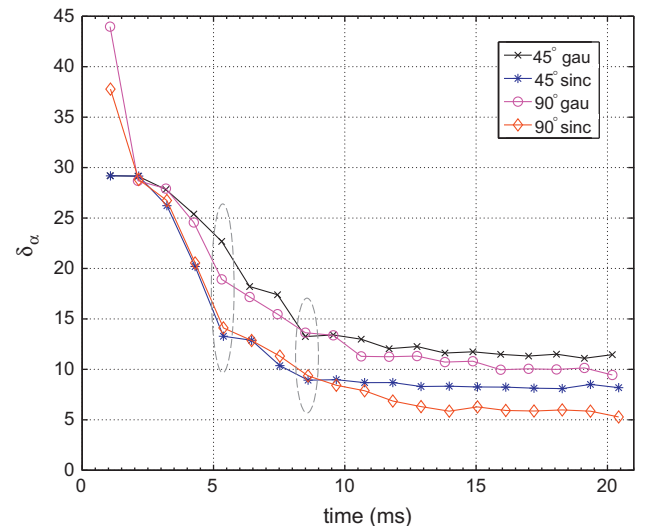
Fig. 3. Cost function values (δ_α, Eq. (1)) for non-selective composite pulses as a function of total pulse duration. Each data point represents a unique composite pulse with the different combinations of sub-pulse shape (GAU or SINC) and target flip angle (45° or 90°) indicated by different colors. Dashed ellipses indicate the pulses chosen for in-depth analysis via simulation and experiment. In all cases, the largest degree of cost function improvement is achievable with pulse durations <10 ms, with longer durations only leading to modest performance gains. SINC composites systematically outperform GAU pulses of the same structure while higher flip angles (i.e., 90°) lead to improved cost function values especially for pulse durations >10 ms. (For interpretation of the references to colour in this figure legend, the reader is referred to the web version of this article.)

the only exception being a 1 mm acquisition resolution in the phase-encoding direction.

3. Results

This section is divided into three parts. Results of all non-selective pulse optimizations are given in Section 3.1. Simulations of pulse performances for both non-selective and slice-selective pulses are presented in Section 3.2. Results of phantom and *in vivo* brain experiments including field maps and slice profile measurements are described in Section 3.3.

3.1. Optimizations

The final cost function values (Eq. (1)) for all non-selective pulse optimizations are given as a function of total pulse duration in Fig. 3. These data contain several noteworthy features. Firstly, regardless of the type of pulse (i.e., 45° or 90°, GAU or SINC), cost function values decrease dramatically as a function of total pulse duration out to ∼10 ms. Beyond this point, improvements in the cost function become increasingly small. Secondly, the SINC pulses result in better performance at any given duration beyond 3 ms. Thirdly, the 90° pulses largely perform better than their 45° counterparts.

Entries encircled by dashed lines in Fig. 3 indicate the pulses selected for in-depth analysis. All further results presented in this paper pertain either to one of these eight pulses or to one of the 1-GAU pulses referred to in Section 2.3. It should be noted that, although these selected pulses represent practical options in terms of duration and performance, they do not reflect the maximum B_1^+-insensitivity (as measured by the cost function) of pulses produced in this study. Further reductions in δ_α of ∼50% are possible when considering longer pulses (e.g., compare the 90° SINC pulses of 8.5 ms and 20.2 ms durations in Fig. 3).

3.2. Simulations

Simulated magnetization responses to both non-selective and slice-selective versions of the designated sub-set of pulses are shown in Fig. 4 (for $\alpha^T = 45°$) and in Fig. 5 (for $\alpha^T = 90°$). In addition to the magnitude of the transverse magnetization ($|M_T|$), these figures contain the non-selective and slice-selective RF modulations as well as the slice-selective gradient waveforms. Magnetization uniformity within the optimized regions on the B_1^+-ΔB_0 grids is greatly improved (with respect to the 1-GAU pulses) through the use of optimized composite pulses, and the degree of uniformity appears to correlate with the cost function values reported in Fig. 3. Moreover, the simulations of slice-selective pulses exhibit similar B_1^+-insensitivity to their non-selective counterparts—thus validating, in part, the methods adopted by this study for the generation of B_1^+-insensitive, slice-selective pulses.

Figs. 4 and 5 also illuminate differences in slice profiles resulting from the various pulses. While SINC pulses generally exhibit the greatest B_1^+ insensitivity and a more sharply defined central excitation region, the anticipated side lobes associated with the use of sinc-center pulses (Fig. 2) are apparent in the composite pulse simulations. Additionally, some subtle asymmetries in slice profiles can be seen for the 45° pulses. These features are most prominent for the 5-GAU and 8-GAU pulses and appear to correlate with the degree of asymmetry along the ΔB_0 direction in the magnetization plots for the corresponding non-selective pulses.

While the composite pulses largely reflect the desired degree of B_1^+-insensitivity, there are some complications with such pulses that become apparent through the simulated magnetization responses. Perhaps most significant is the introduction of non-linear

through-slice phase (see Fig. 6). This effect is most prominent in the waveforms with the highest integrated amplitudes and at the highest $B_1^+/B_{1,\text{nom}}^+$ values (e.g., the 90° 8-SINC pulse). The detriment of non-linear phase is signal loss resulting from residual incoherences in ϕ_{MT} following application of a linear rephasing gradient. Due to this phenomenon, pulses with the lowest cost function values may not always result in the largest signal gains. The results of Fig. 6 indicate that total phase dispersion within the central 2 mm of the slice is $\leqslant \pi/3$ radians in all cases except that of the 90° 8-SINC pulse for which the dispersion is approximately twice as large. The maximum phase dispersion for a particular pulse always occurs at the highest value of B_1^+, while dispersion at lower B_1^+ values is significantly less. Also noteworthy is the observation that even 1-GAU pulses do not result in perfectly linear through-slice phase, although the relative level of dispersion is quite small. Additionally, non-linear phase is in general more prominent at higher flip angle.

Results of simulations for a ±200 Hz range of off-resonance values are presented in Figs. 7 and 8, which show $|M_T|$ and ϕ_{MT}, respectively. For the sake of brevity, results are given only for the 90° 5-GAU pulse. In Fig. 7, $|M_T|$ appears largely stable out to the prescribed limits of ±150 Hz. At and beyond this range, the slice profile deteriorates significantly, mirroring non-uniformities in $|M_T|$ beyond the optimization region for the corresponding non-selective pulse (see Fig. 5). This observation further validates the proposed methods for slice-selective, B_1^+-insensitive pulse design in that the ΔB_0 range targeted in the optimization of non-selective pulses translates to a slice-profile stability for the corresponding slice-selective pulses. The simulations of Fig. 8 indicate that through-slice phase within the ±150 Hz optimization region remains highly linear at lower values of B_1^+. At higher B_1^+ values there exist some noticeable deviations from linearity such as at −50 Hz and −100 Hz; however, the largest deviations from linearity are confined to off-resonance values beyond the optimization range, suggesting that the optimization in some way promotes the desired behavior. Although described specifically for the 90° 5-GAU pulse, such observed off-resonance behaviors were found to be largely representative of the other seven composite pulses detailed in this study.

Further simulation results involve the effects of T_2^* decay on $|M_T|$ during execution of a given excitation pulse and are presented in Fig. 9. Values of $|M_T|$ are calculated for a T_2^* value of 30 ms—which reflects an approximate whole-brain mean value at 7 T [24]—and are reported as ratios to the same quantities as calculated for $T_2^* = \infty$. For the 1-GAU pulses, this ratio is ∼98% due to the short duration (∼1 ms) and is found to be independent of B_1^+ intensity. For the 5-GAU and 8-GAU pulses the ratio decreases to ∼90–95% and ∼80–90%, respectively, with $|M_T|$ loss being noticeably greater for the 90° pulses. While additional loss of $|M_T|$ is expected for the 8-GAU pulses relative to the 5-GAU pulses due to the extended duration, the same effect is not necessarily expected to depend on α^T. Furthermore, SINC pulses appear to be less susceptible to T_2^* decay as compared to their GAU counterparts. Specifically, $|M_T|$ is reduced to ∼93% for the 5-SINC pulses and to the range of ∼90–98% for the 8-SINC pulses. Again, the 45° pulses appear to suffer from less $|M_T|$ losses as compared to the 90° pulses, although the difference is quite subtle in the case of 5-SINC pulses. For all composite pulses, $|M_T|$ loss depends to some degree on B_1^+, with the greatest losses generally occurring at high values of B_1^+. Possible explanations and implications of the above T_2^*-related phenomena are left for the discussion.

Table 1 provides values of $\int |A|^2 dt$, $T_{R,\text{min}}$, and $T_{E,\text{min}}$ for the pulses in Figs. 4 and 5. These numbers imply that composite pulses result in significantly (anywhere from ∼5 to 25 times) higher SAR values for a given T_R and minimal possible echo times that are approximately doubled as compared to the 1-GAU pulses of the same flip angle.
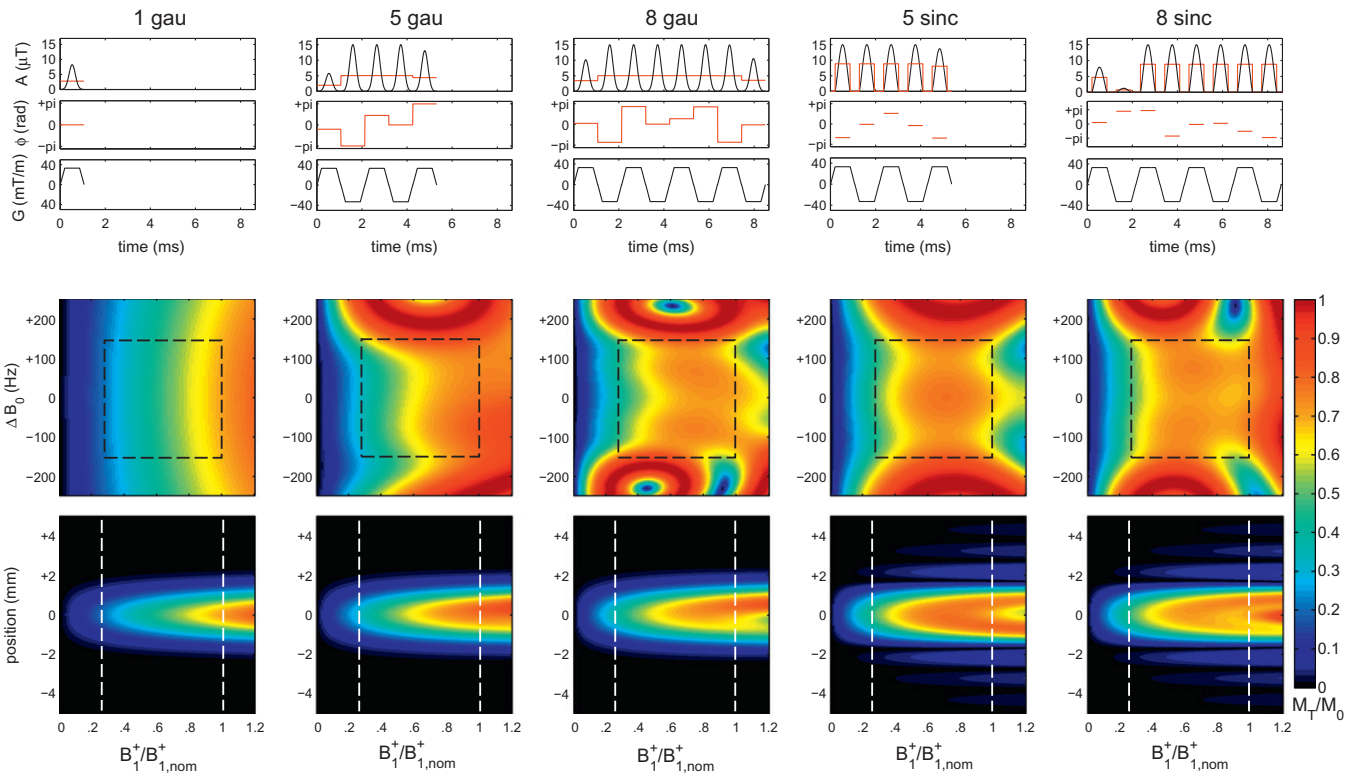
Fig. 4. Amplitude, phase, and gradient modulation waveforms (top row) along with transverse magnetization responses for non-selective (second row) and slice-selective (third row) pulse configurations. At top, non-selective waveforms are designated by red lines and slice-selective waveforms by black lines. All results shown here are for a nominal flip angle of 45° with the selected pulses indicated by dashed ellipses in Fig. 3. In addition to these four pulses is a 1-GAU pulse (far left column) included to illustrate the performance of a B_1^+-sensitive modulation with relatively high-bandwidth. Dashed lines on the magnetization plots indicate the relevant optimization limits for the non-selective pulses. Optimized pulses in both the non-selective and slice-selective forms show improved B_1^+-insensitivity as compared to the single-block/1-GAU pulse. (For interpretation of the references to colour in this figure legend, the reader is referred to the web version of this article.)
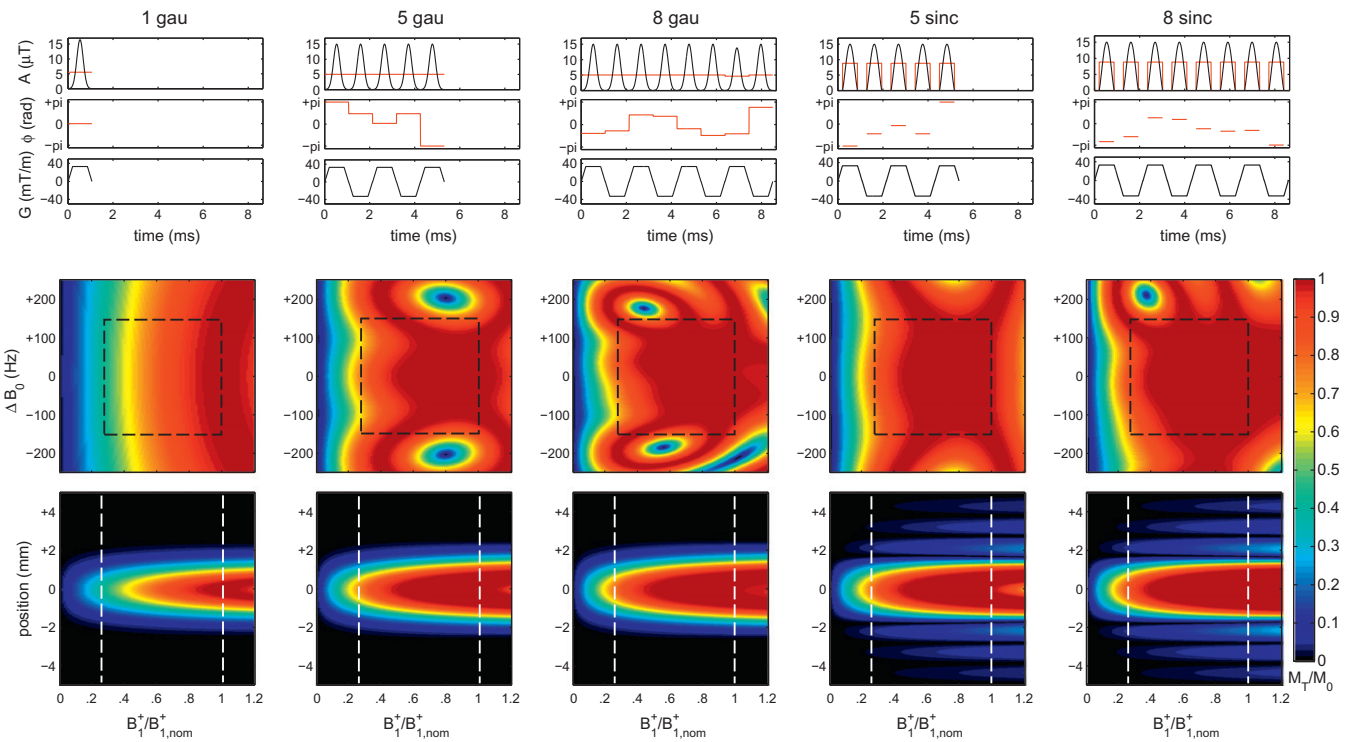
Fig. 5. RF and gradient waveforms and magnetization plots as shown in Fig. 4 but for selected 90° pulses. As for the corresponding 45° pulses, the SINC composites exhibit better immunity to field variations than do the GAU composites but at the expense of prominent lobes in the sidebands of the slice profiles. (For interpretation of the references to colour in this figure legend, the reader is referred to the web version of this article.)
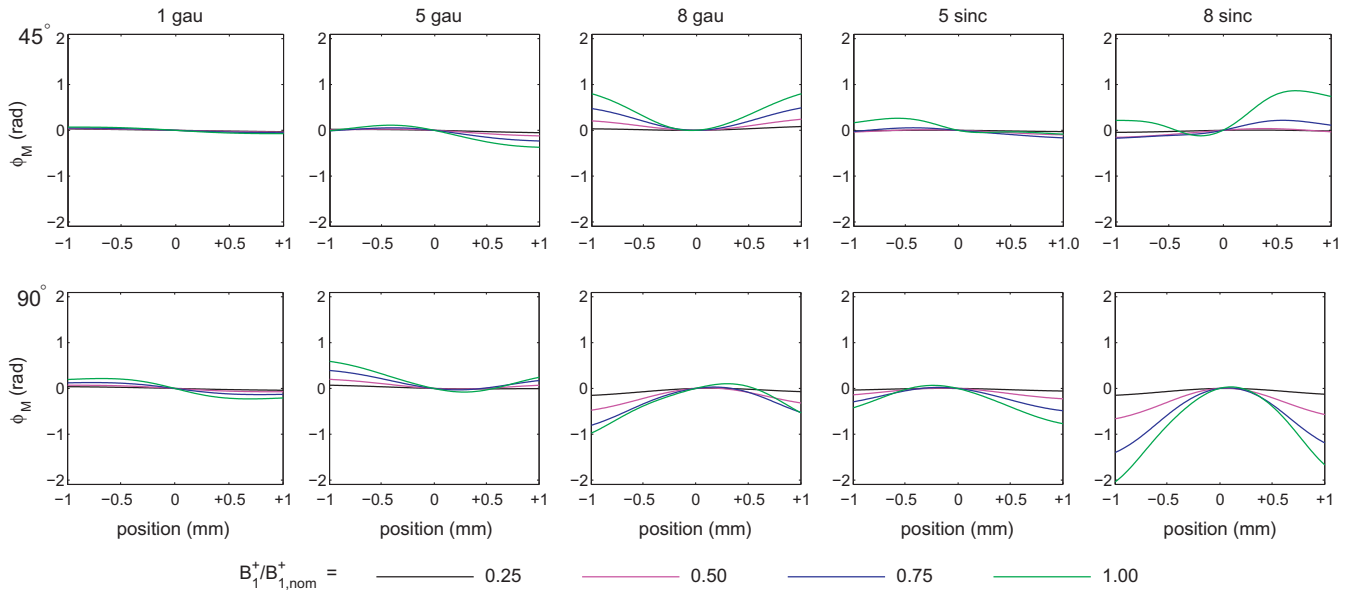
Fig. 6. Non-linearities in through-slice phase of the transverse magnetization after application of rephasing gradients for both the 45° pulses in Fig. 4 (top) and the 90° pulses in Fig. 5 (bottom). 1-GAU pulses (far left) result in a low level of phase non-linearity which generally increases with the presence of additional sub-pulses. For a given pulse, the degree of phase non-linearity is strongly dependent on the relative magnitude of the B_1^+ field strength as indicated by different line colors, with most linear phase distributions always occurring at low B_1^+. Out of these examples, only the non-linearities exhibited by the 90° 8-SINC pulse are likely to become a serious performance issue in terms of signal loss, and, even in this case, the troublesome phase dispersions are confined to $B_1^+/B_{1,nom}^+ \geqslant 0.5$. (For interpretation of the references to colour in this figure legend, the reader is referred to the web version of this article.)

3.3. Experiments

Maps of ΔB_0, B_1^+, and $M_0 B_1^-$ for central axial slices of the phantom and three human subjects are shown in Fig. 10. These measurements reflect values consistent with the field variations encompassed by the B_1^+-ΔB_0 optimization grid.

Results of phantom imaging experiments using the same 10 pulses appearing in Figs. 4 and 5 are presented in Fig. 11. Included are both normalized signal intensities and calculated values of the flip-angle dependent function F as described in Section 2.3. While signal intensity variations are visibly reduced through the use of B_1^+-insensitive composite pulses (relative to those of the 1-GAU pulses), it should be noted that even the most uniform excitation would still result in large signal variations due to inhomogeneities in the B_1^- field. Examination of F maps indicates that all tested composite pulses result in improved excitation uniformity with respect to 1-GAU pulses; however, in accordance with simulations, results do vary significantly depending on pulse composition and target flip angle. For example, F maps for 90° pulses generally display less variation than those for 45° pulses.

When limiting comparisons to a given flip angle, SINC pulses are found to produce more uniform excitations at 45° than do GAU pulses—a result predicted by simulations. Although all composite excitations are fairly uniform in the 90° case, the degree of performance variations anticipated from cost function values for the corresponding pulses are not observed. This effect could be caused by a combination of increased levels of non-linear through-slice phase for the SINC pulses and the fact that cost function values reflect performance at a wider range of ΔB_0 values than actually occurs in the phantom. In at least two cases—namely the 45° 5-SINC and 90° 8-SINC pulses—prominent "holes" can be seen in the center of the F maps. These features are likely due to non-linear phase at high B_1^+ in the latter case and a combination of non-linear phase and slice profile deterioration in the former case. While such magnetization responses are certainly undesirable in the context of slice-selective excitation, it should be noted that the B_1^+ values reached in the center of the phantom (Fig. 10) are beyond the corresponding optimization limits.

Slice profiles as measured in the phantom are presented in Fig. 12 for the same 10 pulses detailed previously. These results are consistent with the simulated slice profiles shown in Figs. 4 and 5. As might be expected, the composite GAU pulses produce slice profiles comparable to those of the 1-GAU pulses. Broadening at the base of the SINC profiles likely results from the presence of the side-lobes indicated in the simulations, with this feature becoming slightly more prominent at the higher flip angle. In
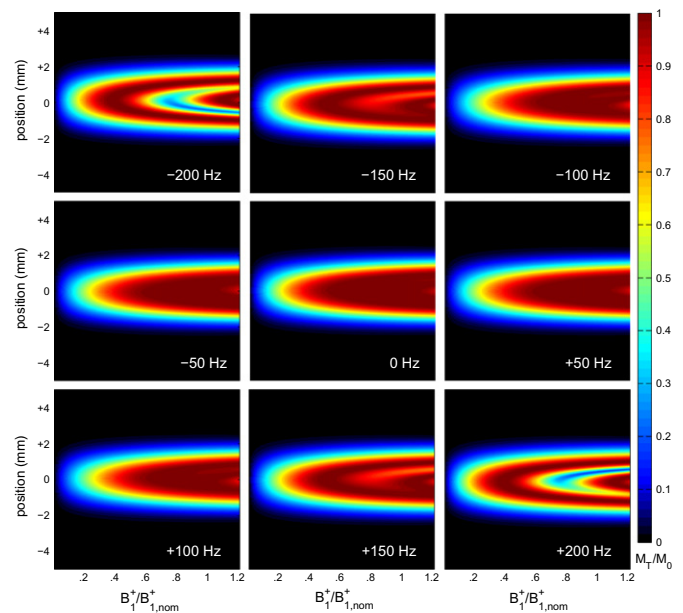
Fig. 7. The slice profile of the 90° 5-GAU pulse as simulated for a ±200 Hz range of frequency offsets. The profile is largely unchanged within the optimization region of ±150 Hz at and beyond which significant deterioration is noticeable. This behavior echoes the magnetization response for the corresponding non-selective pulse as shown in Fig. 5. (For interpretation of the references to colour in this figure legend, the reader is referred to the web version of this article.)
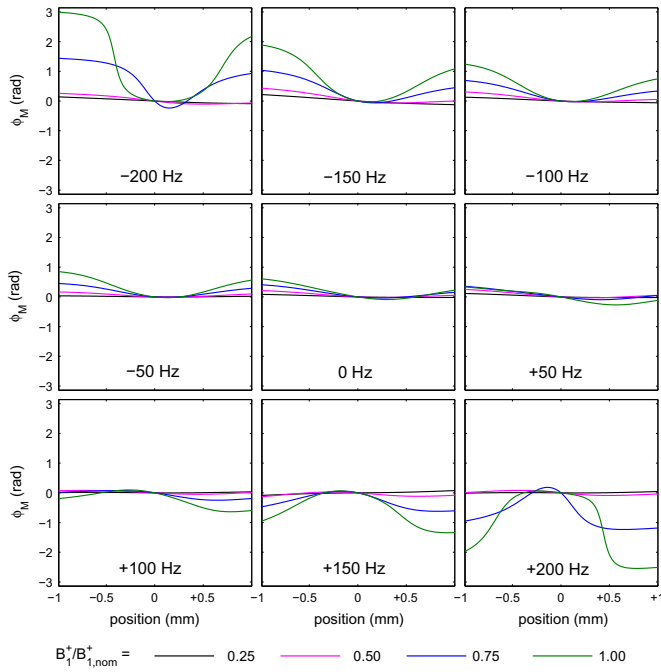
Fig. 8. The transverse magnetization phase of the 90° 5-GAU pulse as simulated for a ±200 Hz range of frequency offsets. On resonance, the phase is highly linear for values of $B_1^+/B_{1,nom}^+$ ranging from 0.25 to 1.00 (see color legend). At and beyond the optimization limits of ±150 Hz, phase non-linearities become prominent, particularly at high B_1^+. (For interpretation of the references to colour in this figure legend, the reader is referred to the web version of this article.)

general, results indicate that the targeted slice thickness of 2 mm is achieved in all cases and that highly selective excitation is possible with the proposed composite pulse designs.

Maps of F calculated from *in vivo* data acquired with the 90° 1-GAU and 5-SINC pulses are shown in Fig. 13 for all three human subjects. In all cases, the composite pulse resulted in significant improvements in flip-angle uniformity, and thus appear to be

functioning as designed in this regard. Moreover, F maps appear to be stable with respect to the range of B_0 variations existing in the brain—an observation that helps establish the validity of requiring immunity to ΔB_0 inhomogeneity through the proposed pulse design protocol.

4. Discussion

Simulations and experiments have validated the proposed pulse design methods as means for the practical construction of slice-selective composite pulses with inherent insensitivity to the field variations observed in the human brain at 7 T. The pulse designs of this study provide a significant advantage over some existing field-insensitive designs in that selective excitation of thin slices is achieved in tandem with prescribed degrees of B_1^+- and ΔB_0-insensitivity. Furthermore, pulses can be designed and implemented for use on any subject or slice orientation without the need for subject-specific field mapping, as is the case for multi-transmit RF shimming and sparse spokes designs. The pulse design protocol allows for designation of arbitrary flip angles and, as long as the resonant offset is not too great, results in only small deviations from a linear through-slice phase of the transverse magnetization. There exist pulse designs for addressing these needs individually, but the strength and usefulness of the proposed design is the incorporation of all such requirements into a single protocol. Adiabatic pulses have been used for achieving immunity to B_1^+ variations for more than 20 years but either lack the capacity for linear phase and arbitrary flip angles (e.g., hyperbolic secant pulses [25,26]) or are not suitable for slice selection (e.g., BIR-4 pulses [2]). The BISS-8 pulse of de Graaf et al. [27], the slice-selective BIR-4 pulses of Balchandani et al. [8], and the more recent adiabatic SLR pulses of Balchandani et al. [28] are examples of adiabatic waveforms that overcome some of these limitations, yet the power requirements required to maintain adiabaticity may prove prohibitive when the goal is excitation in 7 T human imaging. The pulses of the present study may circumnavigate this issue to some extent in that flip-angle uniformity is the optimization criteria rather than the condition of adiabaticity. Thus, improvements in flip-angle
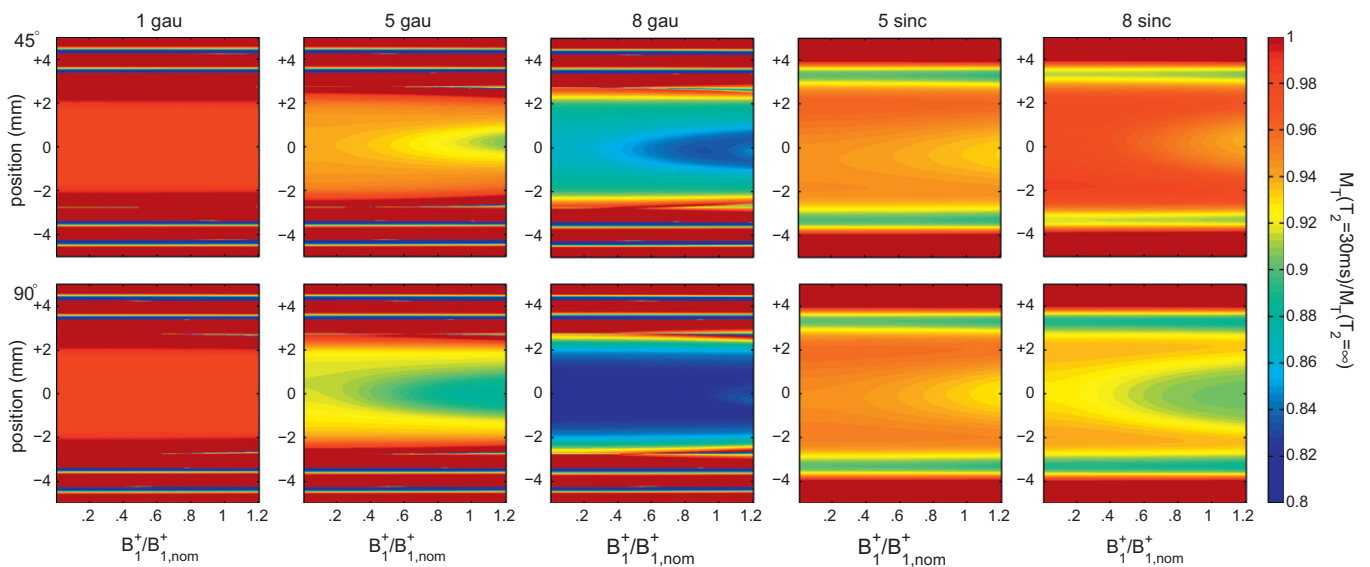

Fig. 9. Simulations of T_2^*-related transverse magnetization losses for the same 45° (top row) and 90° (bottom row) pulses in Figs. 4 and 5, respectively. The ratio of transverse magnetization as calculated for a T_2^* value of 30 ms to that calculated for infinite T_2^* is shown for each pulse. Simulations are performed for the slice-selective versions of each pulse and reflect transverse magnetization loss as a function of both position in the slice-selection direction and relative B_1^+ magnitude. Results indicate that loss of transverse magnetization due to T_2^* decay is not a simple function of total pulse duration, particularly in the case of SINC waveforms. Moreover, T_2^* effects are dependent on the target flip angle and suggest that the ordering of sub-pulses with different amplitudes strongly affects the susceptibility of composite pulses to transverse magnetization decay. (For interpretation of the references to colour in this figure legend, the reader is referred to the web version of this article.)

Table 1
Various quantities pertaining to the practical limitations of selected pulses. Included are the integral of the square of the amplitude modulation (a value directly proportional to SAR, Eq. (5)), the minimum possible T_R value given a SAR constraint of 3 W/kg, and the minimum possible T_E value as described in Section 2.2. SAR levels of composite pulses are as much as 25 times greater than 1-GAU excitations of the same flip angle, a characteristic that is one of the greatest drawbacks to the proposed pulse designs.

α^T	Pulse	$\int |A|^2 dt$ (μT^2 s)	$T_{R,min}$ (ms)	$T_{E,min}$ (ms)
45°	1-GAU	0.017	10	1.6
	5-GAU	0.221	135	2.7
	8-GAU	0.392	239	3.7
	5-SINC	0.324	197	2.7
	8-SINC	0.421	257	3.7
90°	1-GAU	0.068	42	1.6
	5-GAU	0.283	173	2.7
	8-GAU	0.445	271	3.7
	5-SINC	0.335	204	2.7
	8-SINC	0.536	327	3.7
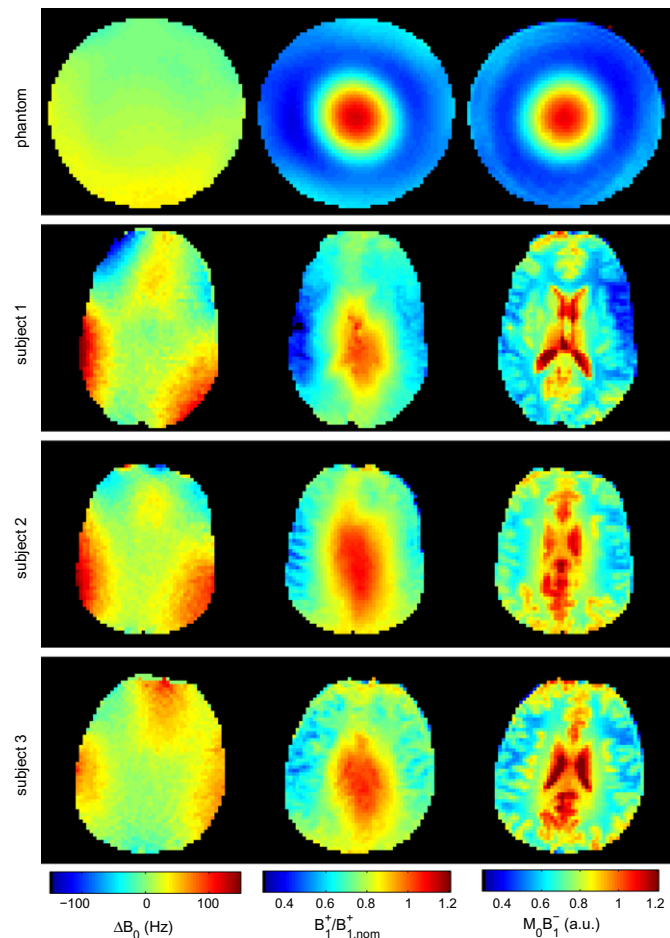
Fig. 10. Measured maps of the static field (left), the transmitted RF field (middle), and the product of equilibrium magnetization and the received RF field (right) are shown for central axial slices through a spherical phantom (top row) and three different human brains (bottom rows). (For interpretation of the references to colour in this figure legend, the reader is referred to the web version of this article.)

uniformity may be realized even when design constraints make the adiabatic condition impossible to satisfy.

While the adiabatic pulses of Balchandani et al. provided the original motivations for the present investigation, recent publications by Matson et al. [16] and Boulant et al. [17] describe more closely related classes of spatially selective, B_1^+-insensitive pulses. These latter studies differ from the present study in some basic aspects of design (e.g., the adoption of the formalism of average Halmiltonian theory and the use of both frequency and phase modulation) but share the common goal of producing field-insensitive, slice-selective excitations for practical high-field imaging sequences. The present study not only corroborates the findings of these previous works but also offers many significant contributions to the body of knowledge regarding the given class of composite pulses. Novel aspects of the present study include: (1) demonstration that a single composite pulse can improve flip-angle uniformity in multiple subjects without subject-specific optimization; (2) determination of the way pulse performance depends on pulse duration; (3) investigation into the influence of sub-pulse shape on pulse performance; (4) confirmation that such composite pulse techniques can produce slices as thin as 2 mm while adhering to current hardware limitations; (5) exhibition of an alternate design protocol that does not explicitly rely on average Hamiltonian theory or frequency modulation; (6) illustration through simulations that T_2^* effects for the given class of pulses depend not only on total pulse duration but also on the shape and amplitude of sub-pulses. These new insights further illuminate important strengths and limitations of the given class of pulses and should prove valuable in determining the suitability of such pulses for high-field human imaging.

Results indicate that composite pulses constructed from SINC sub-pulses outperform their GAU counterparts in terms of insensitivity to field variations. This inherent advantage of the SINC sub-pulses designed for this study arises from a ~10% larger integrated amplitude that such waveforms have when compared to GAU sub-pulses with the same peak amplitude and bandwidth. The larger integrated amplitude translates to higher allowed amplitudes in the constrained optimization of non-selective pulses and, thus, improved performance in terms of the cost function of the optimization. Drawbacks associated with the use of SINC pulses include the existence of side lobes in the slice profiles and the required dead time during the gradient slew period. Such characteristics of SINC sub-pulses raise the question of how to redesign sub-pulses such that the integrated amplitude is maintained and the slice profile sharpened without considerable increase in pulse duration. The Shinnar-Le Roux (SLR) algorithm [29] seems well-suited to this aim, as do the time-dependent gradient modulation techniques of Conolly et al. [30]; however, the short sub-pulse durations and high gradient strengths demanded by the present pulse design will likely limit the advantages of these approaches. Nevertheless, valuable future work might involve an analysis of such alternative RF strategies in the context of designing sub-pulses for use in composite waveforms. Findings would certainly be relevant to single- and multi-channel sparse spokes pulses, as are the results of the present study.

Regardless of the shape of sub-pulses, the target flip angle has proven influential on the optimization performance of the pulses presented in this study (especially in the case of total pulse durations $\gtrsim 10$ ms), with lower flip angles proving more challenging (Fig. 3). The fact that this trend is most prominent at longer durations points to the initial conditions of the optimization as a possible culprit. The results of this study suggest that the ideal solutions for such low-flip-angle excitations might not utilize the maximum available power, especially in the case of longer composite waveforms (compare amplitude modulations in Figs. 4 and 5). Thus, purposefully restricting the peak amplitude of the random initial conditions for pulses with long durations and low α^T values could potentially result in better optimization performance. While this is a possible explanation for the observed optimization results, it is also noteworthy that $|M_T|$ values as plotted in Figs. 4 and 5 will always appear biased to α^T values near 90°. This effect is due to the
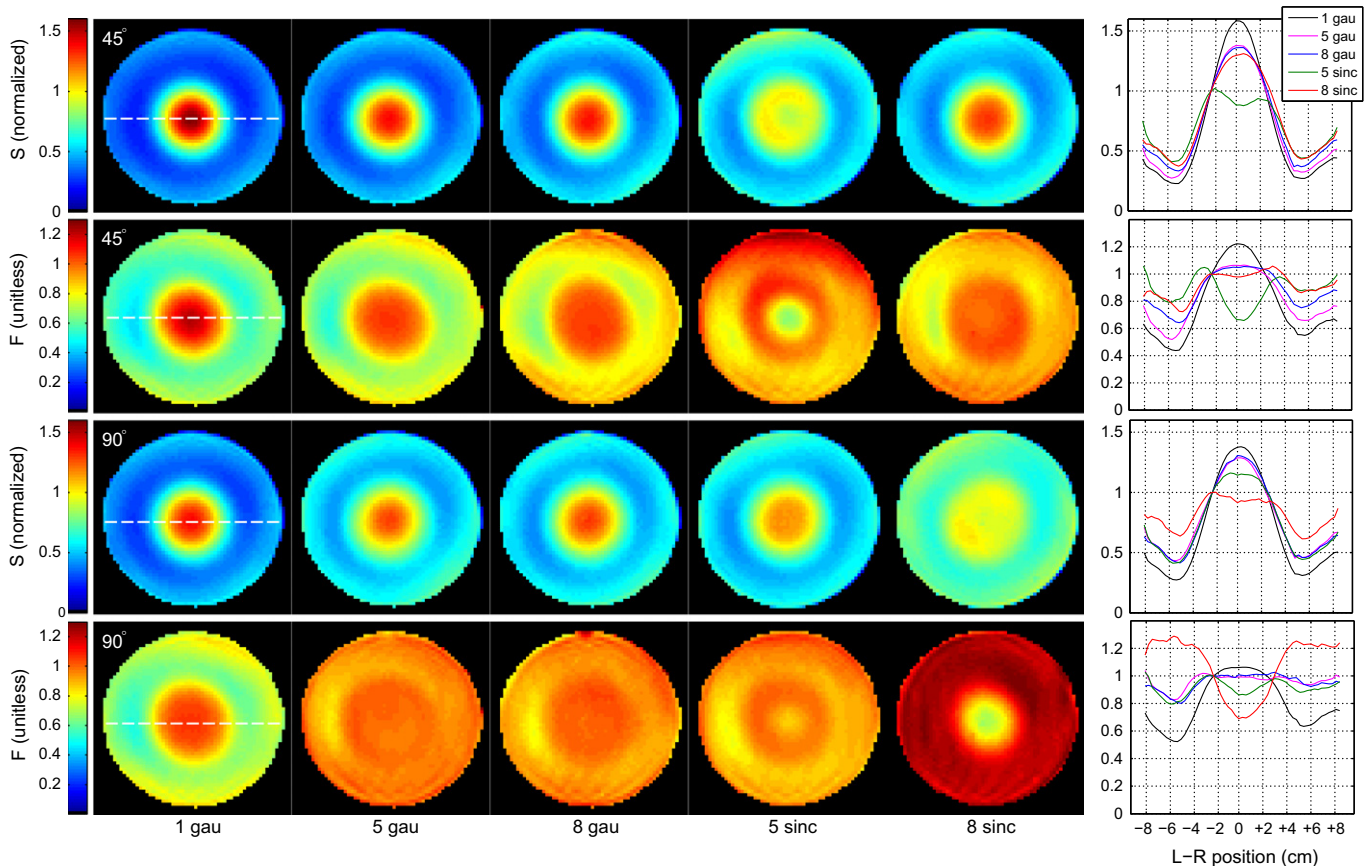
Fig. 11. Experimental results in the phantom at 7 T for the same 45° (top two rows) and 90° (bottom two rows) pulses in Figs. 4 and 5, respectively. The first row for each flip angle shows normalized signal intensity, and the second row shows calculated maps of the flip-angle dependent function *F* as described by Eq. (6). Pulse compositions are indicated at the bottom of each column. Line profiles (far right) reflect values along the position indicated by the dashed line in the far left column. For simplicity, the dashed line does not appear in data for all pulses. While image intensities remain highly varied due to the presence of the inhomogeneous B_1^- field, *F* function distributions reveal the true magnetization responses to the RF pulses and indicate that composite pulses are capable of producing drastically more uniform excitations when compared to the 1-GAU pulses of the same nominal flip angle. (For interpretation of the references to colour in this figure legend, the reader is referred to the web version of this article.)
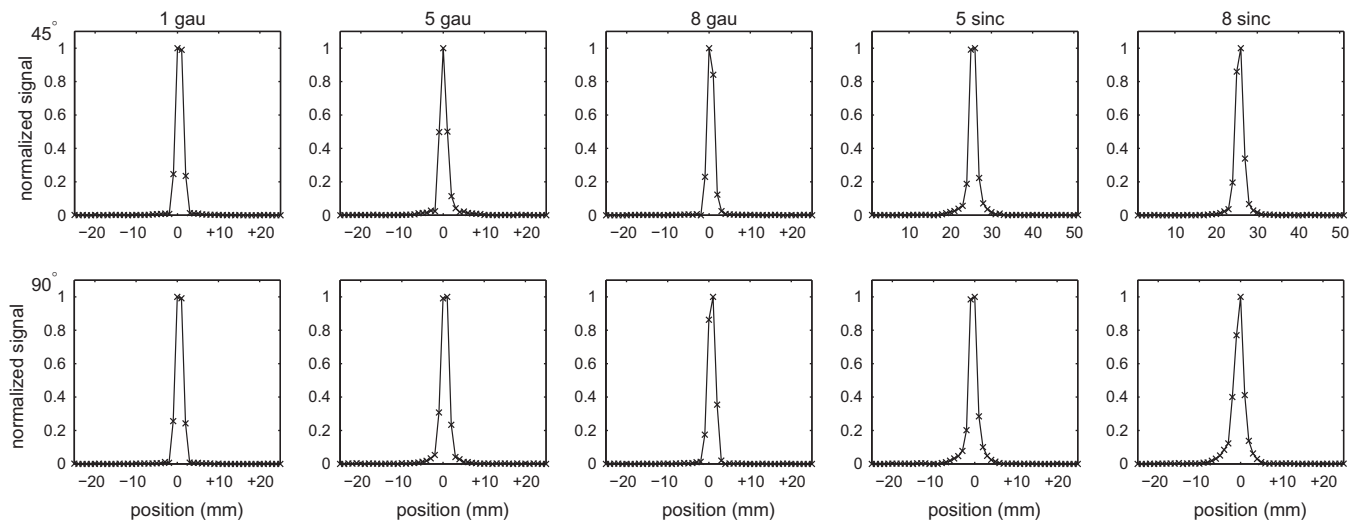
Fig. 12. Slice profiles measured in the phantom for the same 45° (top row) and 90° (bottom row) pulses in Figs. 4 and 5, respectively. Pulse names are given at the top of each column. In all cases, slice thicknesses of ∼2 mm are attained. In agreement with the simulations of Figs. 4 and 5, GAU composites produce cleaner slice profiles than SINC composites, with the latter resulting in a widening of the slice profile base which is likely due to the presence of the side lobes evident in Figs. 4 and 5 for the corresponding pulses.

symmetry of the `sin` function (and thus the transverse magnetization given the relationship $|M_T| = |\sin\alpha|$) around 90° and is independent of the actual cost function values since the cost function is defined in terms of flip angle and not transverse magnetization. This observation suggests that the cost function would possibly be more suitably defined in terms of $|M_T|$ rather than α.
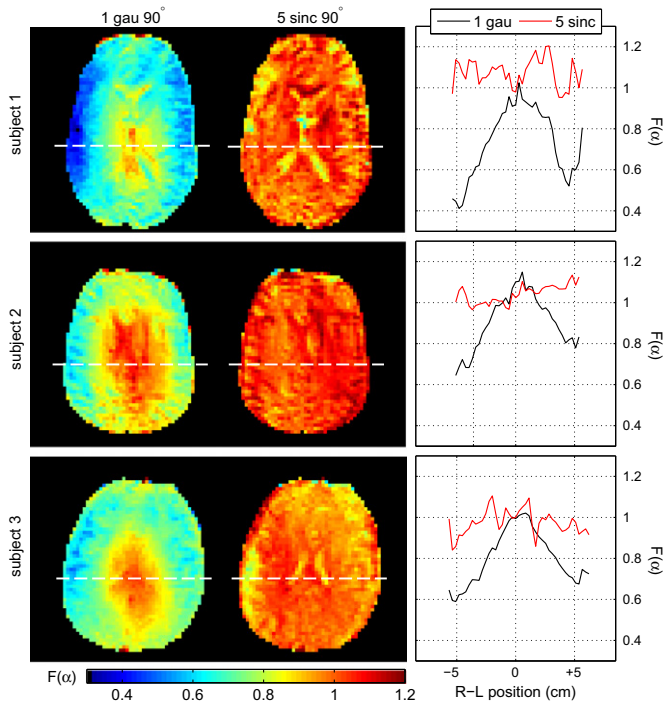
Fig. 13. *In vivo* maps of the flip-angle dependent value F Eq. (6) for the 1-GAU and 5-SINC 90° pulses shown in Fig. 5. F maps are for the central (isocenter) axial slice in three subjects scanned at 7 T with no subject-specific pulse calibrations. Line profiles corresponding to the dashed white lines are given at the far right of each row. These results are in agreement with the phantom results of Fig. 11 and illustrate the degree to which a given B_1^+-insensitive composite pulse can increase flip-angle uniformity across multiple subjects. (For interpretation of the references to colour in this figure legend, the reader is referred to the web version of this article.)

Other results of this study also suggest that alterations to the optimization protocol could result in improved insensitivity to variations in B_1^+ and ΔB_0. For example, the fact that optimized sub-pulse amplitudes are usually near the maximum allowed values suggests that fixing amplitudes and only using sub-pulse phases in the minimization problem might ease the demands on the optimization algorithm and result in better performance [31], or at least performance that is less sensitive to initial conditions. The use of peak amplitudes higher than 15 μT, as is currently supported by the coil/amplifier combinations of some human scanner manufacturers, would certainly result in improved optimization performance. Higher gradient slew rates (>166 T/m/s) are also currently available on human scanners and will only serve to shorten the duration of the SINC version of proposed composite pulses, thereby making pulses less susceptible to T_2^* effects. The possible detriments of higher slew rates are generation of image artifacts caused by gradient-induced eddy currents and an increased likelihood of peripheral nerve stimulation [32].

The levels of non-linear phase reported in Fig. 6 are not prohibitive in terms of signal loss; however, the fact that non-linear phase increases with the number of sub-pulses suggests that the effect may become a more serious limitation for pulses of longer duration (e.g., >10 ms). Furthermore, the largest phase dispersions for a given pulse are always observed at the highest B_1^+ values; therefore, the given class of composite pulses may increase signal in low-B_1^+ regions at the expense of decreasing signal in high-B_1^+ regions. Some phantom results appear to exhibit such high-B_1^+ signal losses (Fig. 11), but the same is not evident for *in vivo* results (Fig. 13). This discrepancy is due to the higher peak B_1^+ values observed in the phantom (Fig. 10) and suggests that signal loss from non-linear phase is not a major concern for practical human brain imaging—at

least for the <10 ms pulses subjected to detailed analysis in this study. Nevertheless, the level of non-linear phase in this class of composite pulses might be controllable through alteration of the cost function and may be relevant to future studies.

The signal losses due to T_2^* decay reported in Fig. 9 offer insights into the advantages of certain pulse constructions. Clearly, SINC pulses result in reduced $|M_T|$ losses with respect to comparable GAU pulses. This observation also holds true with respect to GAU pulses of shorter total duration (e.g., compare the 8-SINC pulses to 5-GAU pulses in Fig. 9). Thus, while SINC composites may incur the penalties of additional non-linear phase and higher SAR, the use of this sub-pulse modulation has the considerable advantage of reduced susceptibility to T_2^* effects. Similar effects have been previously documented in the context of adiabatic pulses, with the resulting decay of $|M_T|$ being characterized by the time constant $T_{2,\rho}$ [18,19].

The observation that 45° composite pulses are less susceptible to collective T_2 effects than are comparable 90° pulses (Fig. 9), suggests that the amplitudes of sub-pulses at the beginning of the composite pulse are critical in determining the amount of T_2^* decay that is possible. As evidenced by the 8-SINC pulses in Figs. 4 and 5, the reduced amplitude of the first two sub-pulses of the 45° pulse (with respect to the 90° pulse) appears to translates to the reduced $|M_T|$ loss exhibited by the corresponding pulses in Fig. 9. This explanation is plausible given that small amplitude sub-pulses produce less transverse magnetization thus limiting the amount of decay that is possible through T_2 mechanisms. In future composite pulse designs, attention could be given to this process so as to limit the susceptibility of the resulting pulses to T_2 effects, with relevant constraints even being incorporated into the optimization. Such design considerations are relevant not only to other B_1^+-insensitive composite pulses (e.g., [9,10,33,34]) but also to sparse spokes pulses designed for either single or multiple transmission channels [15].

For long-T_R GRE imaging applications at 7 T, the SAR levels associated with the composite pulses of the present study will not likely be prohibitive, with the most likely compromise being a reduction of the number of slices in a multi-slice acquisition. Even in the case of the 45° pulses, which would likely be utilized in a steady-state sequence with shorter T_R, an Ernst angle of 45° and a T_1 of 1.5 s (as is typically for the brain at 7 T [35]) imply an ideal T_R of ~500 ms, a value greater than the highest $T_{R, min}$ values reported in Table 1. Thus, all of the 45° pulses presented in Table 1 could be implemented in such a single-slice GRE imaging sequence without the need for SAR-related adjustments. Sequences used at 7 T with shorter T_R values would demand lower α^T values, and, at some point, SAR constraints would need to be enforced in the optimization to ensure the practicality of composite pulses for such applications. Of course, SAR constraints are likely to adversely affect pulse performance; however, the severity of this trade-off and the degree to which it affects the usefulness of the resulting composite pulses has not yet been investigated.

5. Conclusion

The results of this study indicate that construction of composite slice-selective pulses via the described techniques can be used to significantly improve flip-angle uniformity in the human brain at 7 T without the need for subject-specific optimizations. Composite pulses with the desired field insensitivities have been shown to permit slice thicknesses of ~2 mm in as little as ~5 ms when operating within the hardware limitations of a commercial 7 T human scanner. While performance in terms of insensitivity to field variations was found to increase with pulse duration, non-linearities in the through-slice magnetization phase were also found to

become larger with duration and may limit the usefulness of longer composite pulses. This work has also demonstrated how pulse performance is dependent on the structure of the component sub-pulses, with central `sinc`-lobe waveforms offering stronger immunity to field variations and T_2^* effects but rougher slice profiles as compared to Gaussian modulations. The proposed pulse designs may prove useful in many contexts in which insensitivity to field variations is desired in conjunction with selective excitation.

Acknowledgments

References

[1] P.-F. Van de Moortele, C. Akgun, G. Adriany, S. Moeller, J. Ritter, C.M. Collins, M.B. Smith, J.T. Vaughan, K. Ugurbil, B_1 destructive interferences and spatial phase patterns at 7 T with a head transceiver array coil, Magn. Reson. Med. 54 (2005) 1503–1518.

[2] R. Staewen, A. Johnson, B. Ross, T. Parrish, H. Merkle, M. Garwood, 3-D FLASH imaging using a single surface coil and a new adiabatic pulse, BIR-4, Invest. Radiol. 25 (1990) 559–567.

[3] M. Garwood, Y. Ke, Symmetric pulses to induce arbitrary flip angles with compensation for RF inhomogeneity and resonance offsets, J. Magn. Reson. 94 (1991) 511–525.

[4] C.S. Poon, R.M. Henkelman, 180° refocusing pulses which are insensitive to static and radiofrequency field inhomogeneity, J. Magn. Reson. 99 (1992) 45–55.

[5] A. Tannús, M. Garwood, Improved performance of frequency-swept pulses using offset-independent adiabaticity, J. Magn. Reson. A 120 (1996) 133–137.

[6] Y. Luo, R. de Graff, L. DelaBarre, A. Tannus, M. Garwood, The return of the frequency sweep: designing adiabatic pulses for contemporary NMR, J. Magn. Reson. 153 (2001) 155–177.

[7] N. Boulant, D. Le Bihan, A. Amadon, Strongly modulating pulses for counteracting RF inhomogeneity at high fields, Magn. Reson. Med. 60 (2008) 701–708.

[8] P. Balchandani, J. Pauly, D. Spielman, Slice-selective tunable-flip adiabatic low peak-power excitation pulse, Magn. Reson. Med. 59 (2008) 1072–1078.

[9] N. Boulant, J.-F. Mangin, A. Amadon, Counteracting radio frequency inhomogeneity in the human brain at 7 Tesla using strongly modulating pulses, Magn. Reson. Med. 61 (2009) 1165–1172.

[10] J. Moore, M. Jankiewicz, H. Zeng, A.W. Anderson, J.C. Gore, Composite RF pulses for B_1^+-insensitive volume excitation at 7 Tesla, J. Magn. Reson. 205 (2010) 50–62.

[11] H. Liu, G.B. Matson, Radiofrequency pulse designs for three-dimensional MRI providing uniform tipping in inhomogeneous B_1 fields, Magn. Reson. Med. 66 (2011) 1254–1256.

[12] Center for Devices and Radiologic Health, Guidance for the submission of premarket notifications for magnetic resonance diagnostic devices, Food and Drug Administration, 2003.

[13] J. Pauly, D. Spielman, A. Macovski, Echo-planar spin-echo and inversion pulses, Magn. Reson. Med. 29 (1993) 776–782.

[14] S. Saekho, C. Yip, D.C. Noll, F.E. Boada, V.A. Stenger, Fast-k_z three-dimensional tailored radiofrequency pulse for reduce $\hat{B}_1$ inhomogeneity, Magn. Reson. Med. 55 (2006) 719–724.

[15] A.C. Zelinski, L.L. Wald, K. Setsompop, V. Alagappan, B.A. Gagoski, V.K. Goyal, E. Adalsteinsson, Fast slice-selective radio-frequency excitation pulses for mitigating $\hat{B}_1^+$ inhomogeneity in the human brain at 7 Tesla, Magn. Reson. Med. 59 (2008) 1355–1364.

[16] G.B. Matson, L.G. Kaiser, K. Young, New slice-selective pulse cascades produsing uniform tipping in inhomogeneous RF fields, Proc. Intl. Soc. Magn. Reson. Med. 15 (2007) 1682.

[17] N. Boulant, M.A. Cloos, A. Amadon, B_1 and B_0 inhomogeneity mitigation in the human brain at 7 T with selective pulses by using Hamiltonian theory, Magn. Reson. Med. 65 (2011) 680–691.

[18] S. Michaeli, D.J. Sorce, I, D, M. Garwood, Transverse relaxation in the rotating frame induced by chemical exchange, J. Magn. Reson. 169 (2004) 293–299.

[19] S. Michaeli, H. Grohn, O. Grohn, D.J. Sorce, R. Kauppinen, C.S. Springer Jr., Exchange-influenced $T_{2\rho}$ contrast in human brain images measured with adiabatic radio frequency pulses, Magn. Reson. Med. 53 (2005) 823–829.

[20] M.A. Bernstein, K.F. King, X.J. Zhou, Handbook of MRI Pulse Sequences, Academic Press, 2004.

[21] M.R. Bendall, D.T. Pegg, Theoretical description of depth pulse sequences, on and off resonance, including improvements and extensions thereof, Magn. Reson. Med. 2 (1985) 91–113.

[22] J. Hornak, J. Szumowski, R. Bryant, Magnetic field mapping, Magn. Reson. Med. 6 (1988) 158–163.

[23] P. Jezzard, R.S. Balaban, Correction for geometric distortion in echo planar images from B_0 field variations, Magn. Reson. Med. 34 (1995) 65–73.

[24] A. Peters, M. Brookes, F. Hoogenraad, P. Gowland, S. Francis, P. Morris, R. Bowtell, T_2^* measurements in human brain at 1.5, 3 and 7 T, Magn. Reson. Imag. 25 (2007) 748–753.

[25] M. Silver, R. Joseph, D. Hoult, Highly selective $\pi/2$ and π pulse generation, J. Magn. Reson. 59 (1984) 347–351.

[26] M. Silver, R. Joseph, D. Hoult, Selective spin inversion in nuclear magnetic resonance and coherent optics through an exact solution of the Bloch-Riccati equation, Phys. Rev. A 31 (1985) 2753–2755.

[27] R.A. de Graaf, K. Nicolay, M. Garwood, Single-shot, B_1-insensitive slice selection with a gradient-modulated adiabatic pulse, BISS-8, Magn. Reson. Med. 35 (1996) 652–657.

[28] P. Balchandani, J. Pauly, D. Spielman, Designing adiabatic radio frequency pulses using the Shinnar-Le Roux algorithm, Magn. Reson. Med. 64 (2010) 843–851.

[29] J. Pauly, P. Le Roux, D. Nishimura, A. Macovski, Parameter relations for the Shinnar-Le Roux selective excitation pulse design algorithm, IEEE Trans. Med. Imag. 10 (1991) 53–65.

[30] S. Connolly, D. Nishimura, A. Macovski, Variable-rate selective excitation, J. Magn. Reson. 78 (1988) 440–458.

[31] T.E. Skinner, K. Kobzar, B. Luy, M.R. Bendall, W. Bermel, N. Khaneja, S.J. Glaser, Optimal control design of constant amplitude phase-modulated pulses: application to calibration-free broadband excitation, J. Magn. Reson. 179 (2006) 241–249.

[32] P.M. Glover, Interaction of MRI field gradients with the human body, Phys. Med. Biol. 54 (2009) R99–R115.

[33] C.S. Poon, R.M. Henkelman, Robust refocusing pulses of limited power, J. Magn. Reson. 116 (1995) 161–180.

[34] J. Moore, M. Jankiewicz, A. Anderson, J. Gore, An optimized composite refocusing pulse for ultra-high field MRI, Proc. Intl. Soc. Magn. Reson. Med. 18 (2010) 2859.

[35] W.D. Rooney, G. Johnson, X. Li, E.R. Cohen, S.-G. Kim, K. Ugurbil, C.S. Springer Jr., Magnetic field and tissue dependencies of human brain longitudinal ^1H_2O relaxation in vivo, Magn. Reson. Med. 57 (2007) 308–318.